

Load-attenuation mechanisms of flexible barrier subjected to bouldery debris flow impact

Abstract The impulse load of boulders at the front of debris flows is critical to the design of structural defense measures, which are commonly constructed on hillsides to mitigate landslide risk. Field evidences have demonstrated the capability of some steel flexible barriers in intercepting debris flows with bouldery inclusions. However, there is still a lack of fundamental understanding of the load-attenuation mechanisms of flexible barriers, especially under bouldery debris flow impact. In this study, systematic tests of mono-disperse and bi-disperse bouldery flows impacting an instrumented flexible barrier were conducted using a geotechnical centrifuge. The impact kinematics and barrier responses, such as mobilized structural forces and elongation of cables, were recorded synchronously. The results reveal that the load-attenuation mechanism of flexible barriers for the frontal impact originates from the barrier deflections and extended interaction duration. Only 30% of the frontal momentum is transferred to the flexible barrier. The performance of the flexible barrier is compared with that of a rigid barrier model under identical testing conditions. It is found that the boulder impulse loads on flexible barrier are significantly attenuated, resulting in a “plateau” pattern of the impact time history. The practical implication is that the design of flexible barriers may not demand separate considerations of the bulk debris and individual boulder impact loads. Detailed examination of the state of debris deposited behind the flexible barrier indicates that the static dry debris is close to the active failure state due to the large barrier deflection.

Keywords Debris flow · Boulder · Flexible barrier · Load-attenuation mechanism · Impact load

Introduction

Flexible steel net barriers are commonly used in mountainous regions to mitigate geological hazards such as rockfalls and debris flows (Wendeler et al. 2006; Bugnion et al. 2012; Sze et al. 2018). Natural boulders or large hard inclusions are ubiquitous within the debris flow body (Fig. 1a) and would become concentrated at the flow front (Johnson et al. 2012). Debris-resisting flexible barriers, developed from rockfall-resisting flexible barriers (DeNatale et al. 1999; EOTA 2016), have been demonstrated to be effective in resisting debris flows with large hard inclusions by some field evidences (e.g., Wendeler et al. 2006). However, the complex boulder-boulder and boulder-fine interactions within the debris flow cause distinct impact mechanisms compared with that of the impact of a single boulder. Although debris fines may serve as a cushioning layer between boulders and barrier to attenuate the impulse loads, Song et al. (2018a) reported that the reverse segregation of graded debris material may result in peak impact force higher than that of a mono-sized boulder flow. There is a dearth of well-documented field monitoring data or well-instrumented physical testing to reveal and quantify the load-attenuation mechanisms of flexible barriers against bouldery debris impact.

Bulk debris impact

Debris flow impact force is one of the key parameters for the design of rigid and flexible debris-resisting structures. The commonly adopted hydrodynamic approach, used for estimating the bulk debris impact force F_d on barriers (Ashwood and Hungr 2016; Hübl et al. 2009; WSL 2009; Kwan 2012; Wendeler et al. 2019), is given as follows:

$$F_d = \alpha \rho v^2 h w \quad (1)$$

where α is dynamic pressure coefficient, ρ is the bulk density of flow (kg/m^3), v is flow velocity (m/s), and h and w are the flow depth and width of the channel (m), respectively. It is implicitly assumed that the flow behaves as a continuum.

Typically, a value of α higher than unity is recommended for design practice. For example, $\alpha = 2.5$ (Kwan 2012) and $\alpha = 2.0$ (Kwan and Cheung 2012) are recommended for the design of rigid and flexible debris-resisting barriers, respectively. A value of α higher than unity (i) accounts for the influence of static load at the base of barrier, which causes force exerted on the barrier higher than the dynamic loading (Song et al. 2017, 2018b) and (ii) implicitly covers some of the impact loads by the entrained boulders at the flow front (Kwan 2012; Kwan and Cheung 2012; Song et al. 2018a); i.e., for rigid barriers, $\alpha = 2.5$ covers the impact loading of boulders up to 0.5 m in diameter, while for flexible barriers, $\alpha = 2.0$ covers the impact loading of boulders up to 2.0 m in diameter. For the design to resist larger boulder impacts, additional loading has to be considered. For rigid barriers, this additional loading can be calculated based on the Hertz contact theory, as briefly described below.

Discrete boulder impact

Aside from the impact load due to bulk debris, the impact loads of boulders entrained within the flow mass is the main cause of structural incapacitation (Fig. 1 b, c; Zeng et al. 2015; Ng et al. 2018) and should be estimated separately. Boulder impact force F_b is estimated using the Hertz contact theory considering plastic deformations within the contact zone (Kwan 2012):

$$F_b = K_c n a^{1.5} \quad (2)$$

$$n = \frac{4r_b^{0.5}}{3\pi(k_b + k_B)} \quad (3)$$

$$a = \left[\frac{5m_b v_b^2}{4n} \right]^{0.4} \quad (4)$$

$$k_b = \frac{1-\nu_b^2}{\pi E_b} \quad (5)$$

$$k_B = \frac{1-\nu_B^2}{\pi E_B} \quad (6)$$



Fig. 1 a Debris flow deposition with granite boulders of varying diameters floating on the free surface in Tianmo Gully, Tibet, China. Alpenstock in the figure has a length of 1.2 m. b Localized punching failure of rigid wall by the impact of a 30-m^3 rock block in Santa Coloma, Principality of Andorra (Mavrouli and Corominas 2010). c Successful interception but failure of a rockfall flexible barrier under the impact of pebble flow, energy dissipating devices (brake rings) not triggered

where K_c is the load reduction factor (0.1 for rigid barrier with consideration of plastic deformations of concrete; Kwan 2012), r_b is the radius of boulders (m), m_b is the mass of boulders (kg), v_b is the velocity of boulders (m/s), E_b is the elastic modulus of boulders (Pa), ν_b is Poisson's ratio of boulders, E_B is the elastic modulus of the barrier (Pa), and ν_B is Poisson's ratio of barrier, respectively.

Through systematic centrifuge modeling of bouldery debris impact on a rigid barrier, Song et al. (2018a) established an explicit criterion for determining the threshold boulder diameter for which the Hertz equation (Eq. 2) should be used for the calculation of boulder impact load. Under this threshold, the bulk debris impact equation (Eq. 1) was found to be sufficient. For example, the bulk debris impact equation (Eq. 1) with an $\alpha = 2.5$ can sufficiently cater for impulses from boulders of 0.6 times of the flow depth. For the design of rigid debris-resisting countermeasures, Song et al. (2018a) defined the critical size of "boulder" entrained in debris flows.

However, for flexible barriers, it is still not clear (i) what the load-attenuation mechanisms of flexible barriers against bouldery debris flows are and (ii) to what extent the boulder impulse loads could be attenuated. As a continuation of Song et al. (2018a), this study conducts physical modeling of bouldery debris impact on an instrumented flexible barrier, with the other test setup unchanged from Song et al. (2018a). By comparing the dynamic response of flexible and rigid barriers, these two questions can be preliminarily answered.

Centrifuge modeling of bouldery debris impact

Scaling principles

Dimensionless groups (Iverson 2015) ensure that the physical processes of modeled and prototype geophysical mass flows are comparable. Open channelized flows are driven downslope by the gravity of the Earth, while the inertial component controls the impact behavior (Chanson 2004). The Froude number Fr

characterizing the inertial forces to the gravitational forces is given as follows:

$$Fr = \frac{v}{\sqrt{g \cos \theta h}} \quad (7)$$

where v is the frontal velocity (m/s), g is the gravitational acceleration (m/s^2), h is the approach flow depth (m), and θ is the inclination of slope. The explicit square form of Fr represents a clearer physical meaning of the inertial and gravitational forces (Song et al. 2018b):

$$Fr^2 = \frac{\rho v^2}{\rho g \cos \theta h} \quad (8)$$

Based on field observations, debris flows can be characterized with Fr ranging from 0 to 7.56 (Costa 1984; Hübl et al. 2009) or even higher.

The Savage number characterizes the ratio of instant grain collision stresses and sustained grain contact shear stresses, and is expressed as follows (Savage 1984):

$$N_s = \frac{\rho \dot{\gamma}^2 \delta^2}{\rho g h} \quad (9)$$

where $\dot{\gamma}$ is the shear rate ($1/s$) and δ is the boulder (particle) diameter (m) of the flow. In addition, the ratio between boulder diameter δ and flow depth h is used as a normalized diameter to quantify the influence of boulder diameter on the impact behavior:

$$N_D = \frac{\delta}{h} \quad (10)$$

In addition, centrifuge modeling ensures that the absolute stress states in the prototype can be reasonably replicated by raising the field of gravity in a model (Schofield 1980; Taylor 1995). Scaling laws relevant to this study (Ng et al. 2016; Song et al. 2018a) are summarized in Table 1.

Model setup and instrumentation

The centrifuge tests in this study were carried out at the Geotechnical Centrifuge Facility at the Hong Kong University of Science and Technology. The 400-g-ton centrifuge has an arm radius of 4.2 m (Ng 2014). A nominal 25 g was adopted in this series of experiments, which corresponds to the position at the base of the model container to the rotating axis. After correction of the effective rotating radius, which is calculated with respect to the center of the model barrier, the effective g-level is 22.4 g (Fig. 2a). The model container has plan dimensions of 1245 mm \times 350 mm and a depth of 851 mm. The Perspex of the model container and a partition wall are used to form a channelized slope within the model container (Fig. 2a). The slope has a channel width of 233 mm (5.2 m in prototype under gravitational condition of 22.4 g) and a length of 1000 mm (22.4 m in prototype), and is inclined at 25° (Song et al. 2018a). Mounted above the model slope is a storage container with a model volume of 0.03 m³. The storage container has a hinged door at the bottom that can be released in-flight using a hydraulic actuator.

A flexible barrier rigid post, 200 mm in height, is mounted 530 mm (11.9 m in prototype) from the most upstream end of the slope and abuts the Perspex (Fig. 2b). The effective width of the flexible barrier is 203 mm (4.5 m in prototype). The rigid post has ball and socket connections to secure each steel strand cable. In total, four cables, namely, top, upper intermediate, lower intermediate, and bottom cables, span horizontally to form the face of the barrier. The other ends of the horizontal cables pass through the partition via pulley systems and are attached to individual spring mechanisms. Each spring mechanism comprises one relaxed and one preloaded compression spring in series.

The load-displacement behavior of different prototype energy-dissipating elements (dashed line in Fig. 2c) was considered in developing the model energy-dissipating element. The complex non-linear loading behavior of the prototype is further simplified as a distinct bi-linear relationship for the loading response of a model barrier horizontal cable (solid line in Fig. 2c). The slope K_1 is steep, representing a stiff elastic response. The point of inflection is analogous to the activation of the energy-dissipating elements in a prototype barrier. After that, the loading curve exhibits a softer response

Table 1 Relevant scaling laws (22.4 g)

Parameter	Dimension	Scaling law (model/prototype)
Gravity	L/T^2	N
Density	M/L^3	1
Length	L	$1/N$
Velocity	L/T	1
Inertial time	T	$1/N$
Stress	$M/(T^2L)$	1
Force	ML/T^2	$1/N^2$
Flexible barrier stiffness	M/T^2	$1/N$

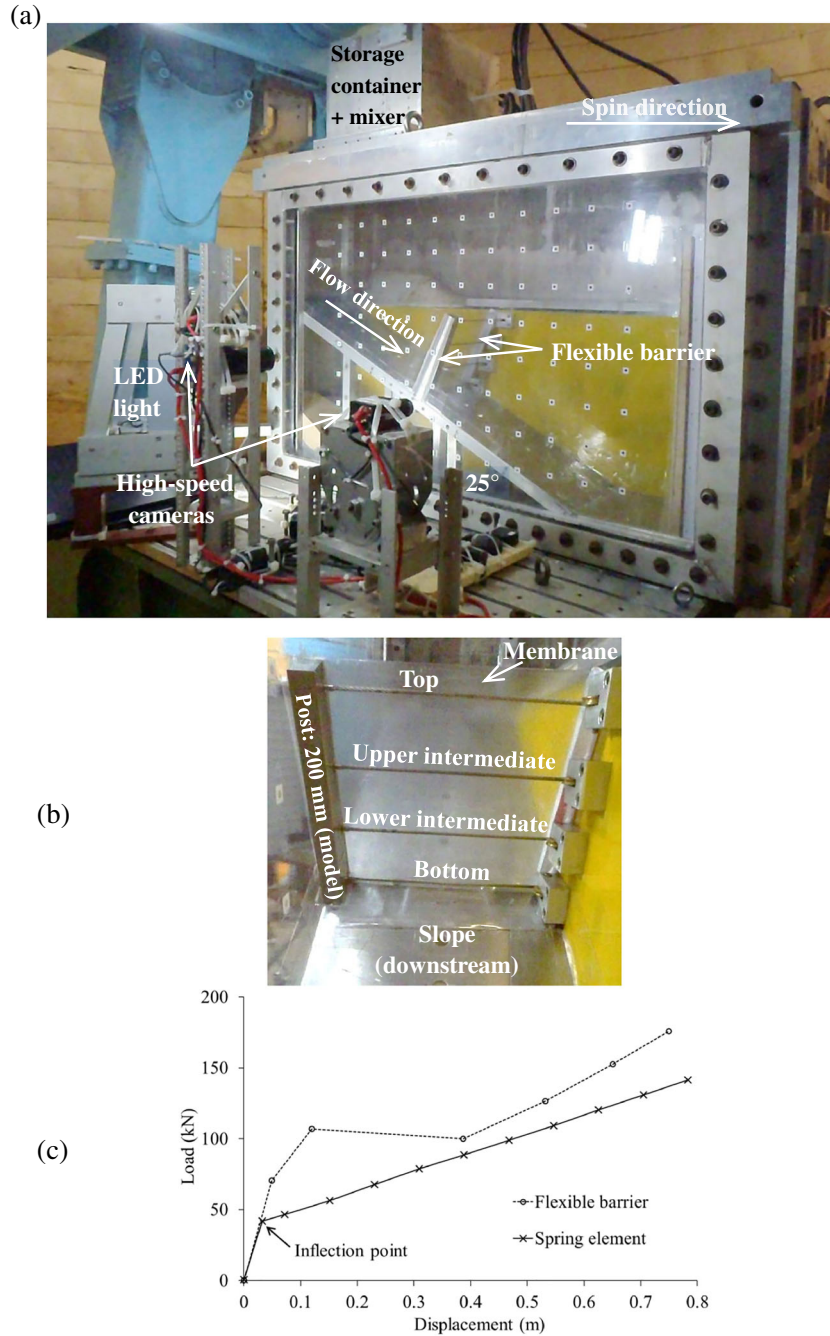


Fig. 2 a Side view of a flexible barrier model setup on centrifuge platform. b Model flexible barrier with rigid post, four horizontal cables, and membrane. c Load-displacement behavior of a flexible barrier cable (Ng et al. 2016, in prototype)

(K_2). Properties of the prototype flexible barrier are summarized in Table 2. A membrane is installed along the upstream face of the flexible barrier to act as a net that simulates the

full retention of debris materials. In the horizontal direction, slack (fold and redundancy) was provided in the high-stiffness membrane to ensure that the membrane would stretch out

Table 2 Properties of flexible barrier (all dimensions in prototype)

Flexible barrier	Stiffness (kN/m)	Inflection point (kN)
Top cable	$K_1 = 2.6 \times 10^3$ $K_2 = 2.0 \times 10^2$	40
Upper, lower intermediate, and bottom cables	$K_1 = 1.8 \times 10^3$ $K_2 = 2.0 \times 10^2$	40

and not be subject to tension under impact. This ensures that the impact load is fully transmitted to the horizontal cables. However, in the vertical direction, since it is difficult to model the relative movement between the net and cables, slack was not provided, implying a stiffer connection between cables. This results in a larger proportion of load transfer between cables as compared with the prototype. We mainly focus on the total impact load in this study, which will not be affected by this model arrangement. The assumptions adopted in this study simplify the actual impact conditions to obtain fundamental insights for improving our understanding of flow-structure interaction. Details of the model flexible barrier system are described by Ng et al. (2016).

Load cells were installed along each horizontal cable to measure the induced axial forces. Laser sensors with a resolution of 0.2 mm were used in conjunction with the spring mechanisms of the flexible barrier model to measure cable displacement synchronously with the force measurement. A high-speed camera with a resolution of 1300×1600 pixels at a sampling rate of 640 fps (Fig. 2a) was adopted to capture the frontal velocity, flow depth, and impact kinematics.

Bouldery debris materials

In this study, the prototype boulder-entrained flows are simplified as mono-disperse glass sphere flows and bi-disperse mixtures of glass spheres and rounded sand. The advantages of using glass spheres are that (i) they have a density comparable to geomaterials like sand (with a specific density around 2500 kg/m^3 and a bulk density of $1500\text{--}1600 \text{ kg/m}^3$), (ii) they have a Young's modulus close to those of materials like granite (60 GPa), (iii) they have a well-characterized diameter (see Eq. 3), and (iv) results should be on the conservative side, since interlocking due to irregular shapes does not occur.

Glass spheres with various diameters and Leighton Buzzard (LB) fraction C sand (Fig. 3) were used to simulate mixed dry bouldery flow fronts. Under elevated gravitational conditions (22.4 g), the particle diameter in the prototype scale corresponds to a diameter 22.4 times that of the model scale (Table 1). Glass spheres with diameter 3, 10, 22, and 39 mm are equivalent to boulders with diameter of 70, 220, 490, and

870 mm, respectively. LB fraction C sand comprises fairly uniform grains with diameters of about 0.6 mm (13 mm in prototype) and has an internal friction angle of $30\text{--}31^\circ$.

Test program and procedure

The centrifuge modeling tests were divided into two steps. Step I (free-flow tests) is for the characterization of the flow regime of the bouldery flows. The model slope was inserted between the Perspex sidewall and the partition without the flexible barrier. In step II, a flexible barrier was mounted for the impact tests. The debris-barrier impact test program is given in Table 3. A total of 7 tests, i.e., mono-disperse (glass spheres) and bi-disperse (glass sphere-sand mixtures) flows, have been conducted. With the use of glass spheres of different sizes, the effects of boulder diameter can be studied. A comparison of flexible and rigid (Song et al. 2018a) barrier test results under identical flow conditions highlights the necessity of investigating barrier stiffness for debris-barrier interaction.

Once the model was prepared, the centrifuge was spun up to 22.4 g. The interaction time was scaled down to $1/22.4$ of prototype condition (Table 1). To account for this, a sampling rate of 20 kHz was sufficiently high to capture the dynamic processes. After readings stabilized, the storage container door was released by the hydraulic actuator. The bouldery flows transitioned onto the slope and impacted the barrier. The cable force, cable elongation, and high-speed imagery were recorded synchronously. After the debris mass reached a static state, the centrifuge was spun down.

Characterization of flow regime

The Froude numbers of the flows are within the range between 2 and 7, which are broadly comparable to those observed in the field (Hübl et al. 2009). The Savage number increases as the glass sphere diameter increases. Using the threshold reported by Savage and Hutter (1989), for $N_S > 0.1$, the flows are in a collisional regime rather than the grain contact regime. The flows are mainly in the collisional state. For flows with $\delta/h = 1.0$, the flow thickness is composed of a single layer of glass spheres. There is no shear rate, so the definition of N_S is no longer valid. The characterization of flow regime is summarized in Table 4.

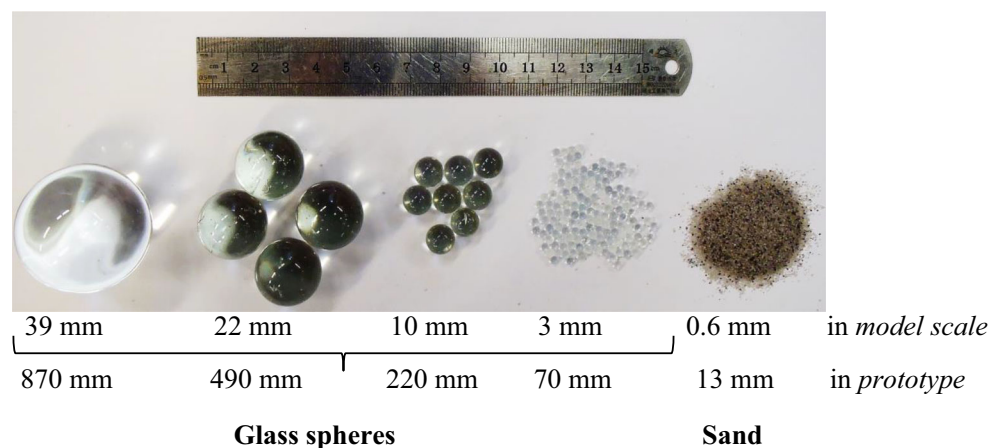


Fig. 3 Debris materials: glass spheres of varying diameters and Leighton Buzzard fraction C

Table 3 Test program of bouldery debris impact (all dimensions in model scale)

Flexible barrier	Test ID Rigid barrier (Song et al. 2018a)	Materials	Dispersity
FB3	RB3	Glass spheres (3 mm)	Mono-disperse flows
FB10	RB10	Glass spheres (10 mm)	
FB22	RB22	Glass spheres (22 mm)	
FB39	RB39	Glass spheres (39 mm)	
FB10S	RB10S	Glass spheres (10 mm) and LB fraction C sand (0.6 mm)	Bi-disperse flows
FB22S	RB22S	Glass spheres (22 mm) and LB fraction C sand (0.6 mm)	
FB39S	RB39S	Glass spheres (39 mm) and LB fraction C sand (0.6 mm)	

Results and interpretation

The results of mono-disperse and bi-disperse boulder flow impact on the flexible barrier are reported in this section. To facilitate comparison, all dimensions are presented in prototype unless stated otherwise. The initial time of all tests (impacts) are readjusted to 1.0 s.

Impact kinematics

Images depicting the typical impact kinematics of mono-disperse flows (FB39, 870 mm in prototype) are shown in Fig. 4. The flow direction is from left to right. As the glass spheres reach the base of the flexible barrier with a velocity of 9.1 m/s, deflection appears in the downstream direction ($t = 1.6$ s, Fig. 4a). After that, the frontal particles form a static load at the barrier base. Subsequent flow overrides the static particles and impacts the upper portion of the barrier ($t = 1.9$ s and 2.2 s, Fig. 4 b, c). Without the regulation (reduction of effective stress) by interstitial fluid (see the two-phase flow impacts in Song et al. 2018b; McArdell et al. 2007), the overall impact process is characterized as a pile-up impact mechanism (Gray et al. 2003; Koo et al. 2016), with many particles accumulating at the upstream end of the flume ($t = 5.0$ s, Fig. 4d). No obvious rebound of the flexible barrier deflection was observed. This implies that the static load dominates in the final stage of impact. Similar observations have been reported by Kwan

et al. (2018) who analyzed the debris-barrier interaction of field tests using the advanced coupled analysis model.

The kinematics of bi-disperse flows is similar with that of mono-disperse flows. It is worth mentioning that the reverse segregation generated in the bi-disperse flows ensures that boulders shift to the free surface and migrate to the front of the flow, as observed in prototype flows (Johnson et al. 2012). As a result, the approaching velocity of boulders is not attenuated simultaneously with the fine sand (see Song et al. 2018a for details). The bi-disperse flows result in lower deposition heights because the fine debris within the voids of boulders enhances the boundary and internal resistance. Test FB39 results in a deposition height of 62% of the barrier height (2.8 m/4.5 m), while test FB39S results in 30% of the barrier height (1.5 m/4.5 m).

Cable elongation and barrier deflection

The large deformation of a flexible barrier is the key feature for attenuating impulse loads by the entrained boulders. The cable elongation of a flexible barrier is crucial for investigating barrier loading behavior and is rarely recorded in the large-scale tests (DeNatale et al. 1999; Bugnion and Wendeler 2010) or field monitoring (Wendeler et al. 2006). The cable elongation of this experimental study is measured synchronously with cable force. Figure 5a shows the measured cable elongation of test FB39 by

Table 4 Characterization of the flow regime

Test ID	Typical particle diameter (mm, prototype in bracket)	Bulk density (kg/m^3)	Free-field flow velocity (m/s)	Froude number (Fr/Fr^2)	Savage number (N_s)	Boulder diameter/flow depth (δ/h)
FB3	3 (70)	1539	14.2	4.7/22.1	0.09	0.07
FB10	10 (220)	1611	21.9	6.7/44.9	1.0	0.2
FB22	22 (490)	1583	9.4	2.7/7.3	0.9	0.4
FB39	39 (870)	1513	9.1	3.3/10.9	Discrete*	1.0
FB10S	10/0.6 (220/13)	1822	11.4	5.0/25.0	3.3	0.4
FB22S	22/0.6 (490/13)	1831	9.1	3.7/13.7	7.0	0.7
FB39S	39/0.6 (870/13)	1818	8.7	3.1/9.6	Discrete	1.0

*Definition of N_s is not valid for flows with single layer of glass spheres, i.e., $\delta/h = 1.0$

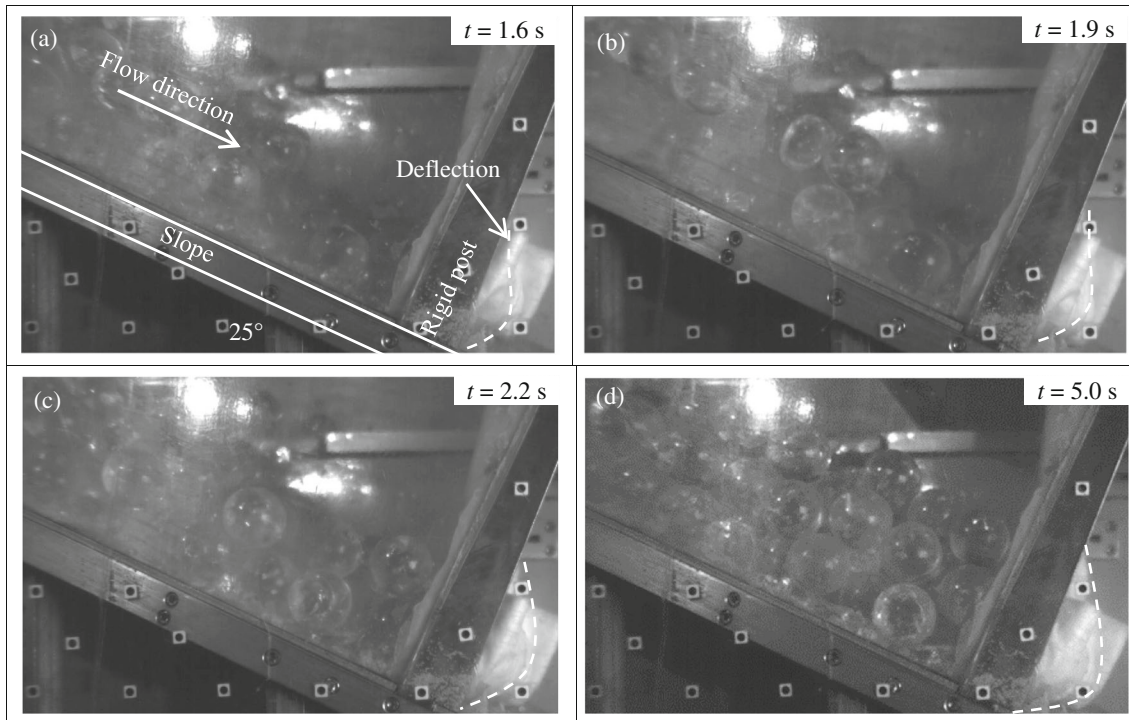


Fig. 4 Observed interaction kinematics of test FB39 in prototype time: **a** $t = 1.6$ s, **b** $t = 1.9$ s, **c** $t = 2.2$ s, and **d** $t = 5.0$ s

the laser sensors. The maximum elongation, 0.55 m (12% of cable length L), occurs in the bottom cable. The elongation decreases with the barrier height, and the upper intermediate and top cables bear negligible elongation.

Impact on the flexible barrier induces substantial barrier deflections (Fig. 4). To deduce the barrier deflections and normal impact load acting on the flexible barrier, a mathematical representation of the deformed horizontal cable is necessary. Since the boulder assembly uniformly distributes along the barrier width and forms pressure perpendicular to the barrier face, a circular curve provides a better approximation of a deformed cable (Fig. 6, Sasiharan et al. 2006). The deflection, D , is defined as the maximum value occurring at the middle of the deformed cable. Based on the geometric relationship (Song et al. 2018b), the maximum deflection D of the four cables can be deduced (Fig. 5b). The trend of deflections is similar with that of cable elongation. However, the maximum deflection of the bottom cable is larger than the corresponding cable elongation, reaching up to 1.0 m in prototype (22% of cable length L).

Cable force and normal impact force

Figure 7a shows the measured cable force time histories of test FB39. The debris only directly impacts the lower portion of the flexible barrier (Fig. 4). As a result, the cable load is mainly concentrated on the bottom and lower intermediate cables. Consistent with the cable elongation measurement (Fig. 5a), the bottom cable is characterized with the maximum cable load. However, due to the interconnection between the four horizontal cables, the upper intermediate and top cables also record relatively lower responses of the impact. Impulses induced by the direct impact

of single 870-mm (39 mm in model scale) boulders are obvious between 1 and 2 s. However, with the growth of static debris at the barrier base, direct impact on the barrier reduces and impulses diminish after 2 s.

As shown in Fig. 6, the decomposition of the cable force T includes a component normal to the barrier face $T_1 (= T \sin \psi)$ and a horizontal component $T_H (= T \cos \psi)$, where ψ is the angle of deflection. The normal components T_1 on the right and left sides of a flexible barrier cable give the impact load induced by the flow, while the horizontal components T_H on both sides counterbalance each other since they are the same in magnitude but opposite in directions. The T_1 time histories for all four horizontal cables are shown in Fig. 7b. The summation of normal components for the four horizontal cables T_1 is the total (resultant) normal impact load F . The horizontal component T_H of the cable force T is shown in Fig. 7c. The summation of the four horizontal components is also shown. Although discrete impulses induced by single boulders are observed, the time histories of normal impact force are characterized as a “plateau” pattern.

Effects of boulder size and barrier stiffness

Mono-disperse flow impact

The total forces of mono-disperse flows with diameters of 70, 220, 490, and 870 mm are summarized in Fig. 8. The total forces of rigid barrier tests conducted by Song et al. (2018a) are also shown for comparison. As can be seen from Fig. 8a to Fig. 8d, with an increase in particle size, the impact forces reflect the transition in impact type, from continuum to discrete loading on the rigid barrier. As the particle size reaches 870 mm in prototype, the peak impulse load

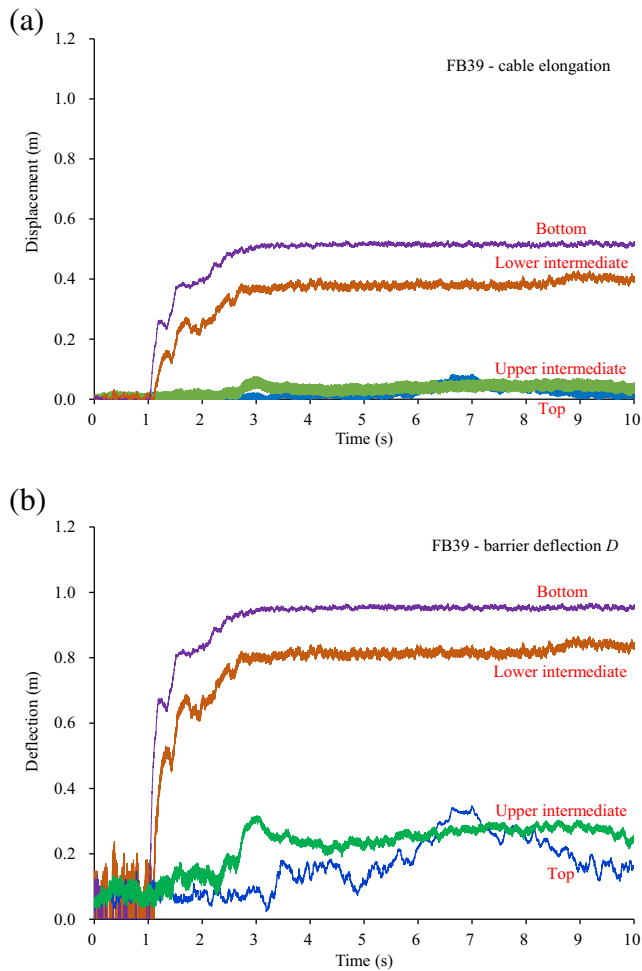


Fig. 5 a Cable elongation and b barrier deflection D of test FB39 (all dimensions in prototype)

on the rigid barrier induced by the frontal boulders is 2900 kN, which is about 6 times that of the static load (Song et al. 2018a).

For the corresponding flexible barrier tests, the peak impact loads on the flexible barrier from boulders are greatly attenuated

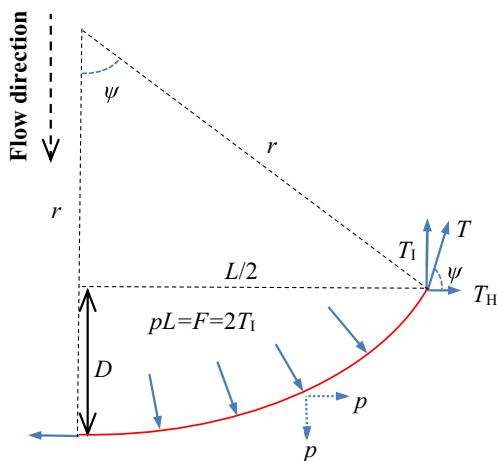


Fig. 6 Diagram of a deflected horizontal cable under distributed load $pL = F$ along the chord of a circular curve (Song et al. 2018b)

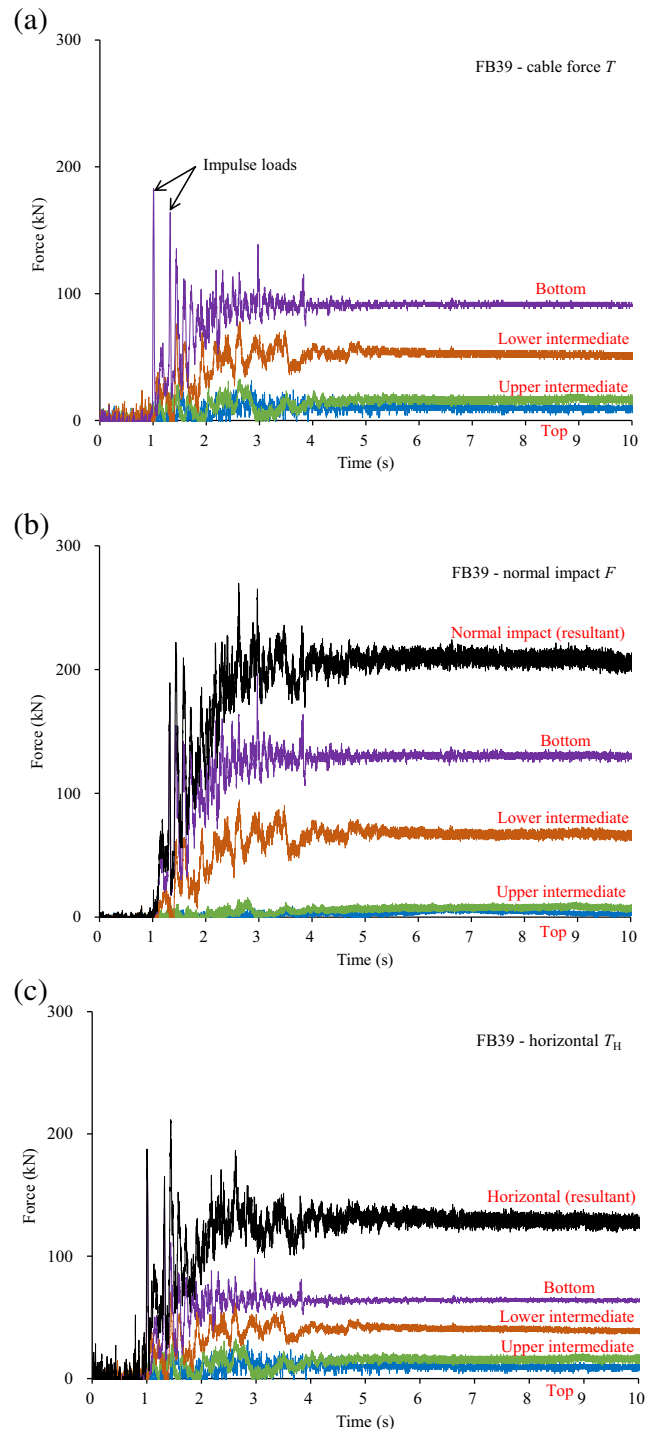


Fig. 7 a Cable force T , b normal impact force F , and c horizontal force T_H time histories of test FB39 (all dimensions in prototype). The total forces of the normal and horizontal force are the summation of the four cable components and denoted as "resultant"

and close to the static loads. The attenuation is especially remarkable for the flows with the largest boulders (870 mm, Fig. 8d). The huge contrast in the dynamic response reflects the effect of barrier stiffness and the engineering significance for adopting flexible barriers in resisting bouldery debris flows.

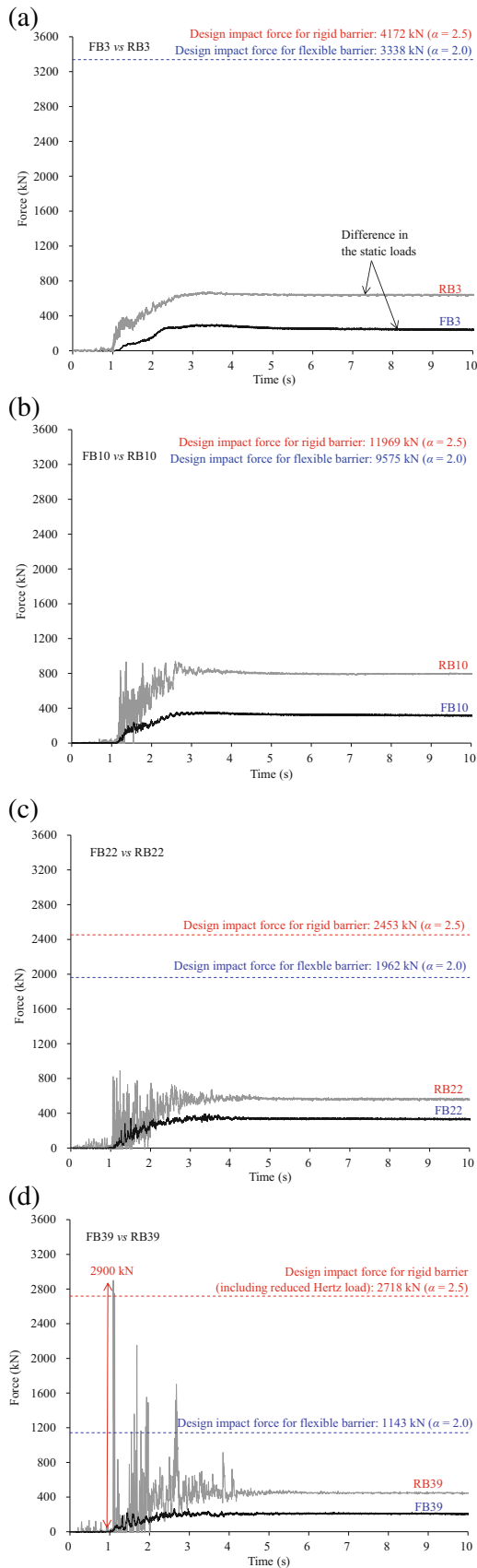


Fig. 8 Comparison of normal impact forces induced by mono-disperse flow impact on flexible and rigid (Song et al. 2018a) barriers: **a** FB3 vs RB3, **b** FB10 vs RB10, **c** FB22 vs RB22, and **d** FB39 vs RB39

Bi-disperse flow impact

When comparing the mono-disperse flow impact loads (Fig. 8) with the bi-disperse flow impact (Fig. 9), the bi-disperse flow impact shows a lower impulse count for both rigid and flexible barrier dynamic responses. This reflects the cushioning effect of the fine material. Like the low stiffness of the flexible barrier, the fine debris in between the boulder and rigid/flexible barrier effectively elongates the interaction duration.

To summarize, the use of flexible barriers to intercept bouldery debris entails two advantages. Firstly, the impulse loads of boulders would be largely attenuated due to the extended interaction duration with the flexible barrier. Debris flow flexible barriers have been developed from rockfall flexible barriers, so it is not unexpected to see the attenuation for a lower barrier stiffness. Second, under otherwise identical conditions, the static loads on the flexible barrier are much lower than those on the rigid barrier. The examination of the state of static debris behind the deflected flexible barrier will be elaborated on in the next section. Both of these two features are obvious from the comparison between the impact loads on flexible and rigid barriers in Figs. 8 and 9.

The impact loads on rigid and flexible barriers are further compared with the design guidelines. The total design impact load is the superposition of both bulk debris (using Eq. (1)) and single-boulder (using Eq. (2)) impact loads. The “Reduced Hertz load” with $K_c = 0.1$ is required for rigid barrier design only if the boulder diameter exceeds 0.5 m (Kwan 2012) when $\alpha = 2.5$ is used for bulk debris impact (see results of tests RB39 and RB39S in Figs. 8d and 9c). The design impact loads derived based on the current design guidelines are generally conservative for rigid barrier, although in tests RB39 and RB39S, the measurements recorded a single spike of transient force above the design impact loads. It should be highlighted that the transient force impulse is more critical on structural damage, which could be better dealt with using the performance-based approach (Yong et al. 2019). For flexible barriers, the measured impact loads are far lower than the predicted bulk debris loads using Eq. (1) with $\alpha = 2.0$. This is consistent with the use of $\alpha = 2.0$ covers a boulder diameter up to 2 m, as recommended by Kwan and Cheung (2012). There is still room for optimization of the current design guidelines of flexible barriers.

Load-attenuation mechanisms of flexible barrier

This section further analyzes the forces exerted on both rigid and flexible barriers in the frontal, peak, and static loading stages. Furthermore, the load-attenuation mechanisms of the flexible barrier are quantified in a dimensionless manner.

Characteristics of frontal impact

The frontal impact is defined as the impact with no obvious dead zone forming at the base of the barrier. Based on the conservation of momentum, the relationship between the force impulse $F\Delta t$ (integration of impact force F over the impact duration Δt) and the change of momentum $m\Delta v$ is analyzed. Figure 10a shows a diagram for calculating the frontal mass m of test RB3. The frontal velocity v_{frontal} obtained from the calibration tests (Table 4) is adopted, and the velocity after impact is assumed to be zero as the frontal mass is either stopped or deflected upwards.

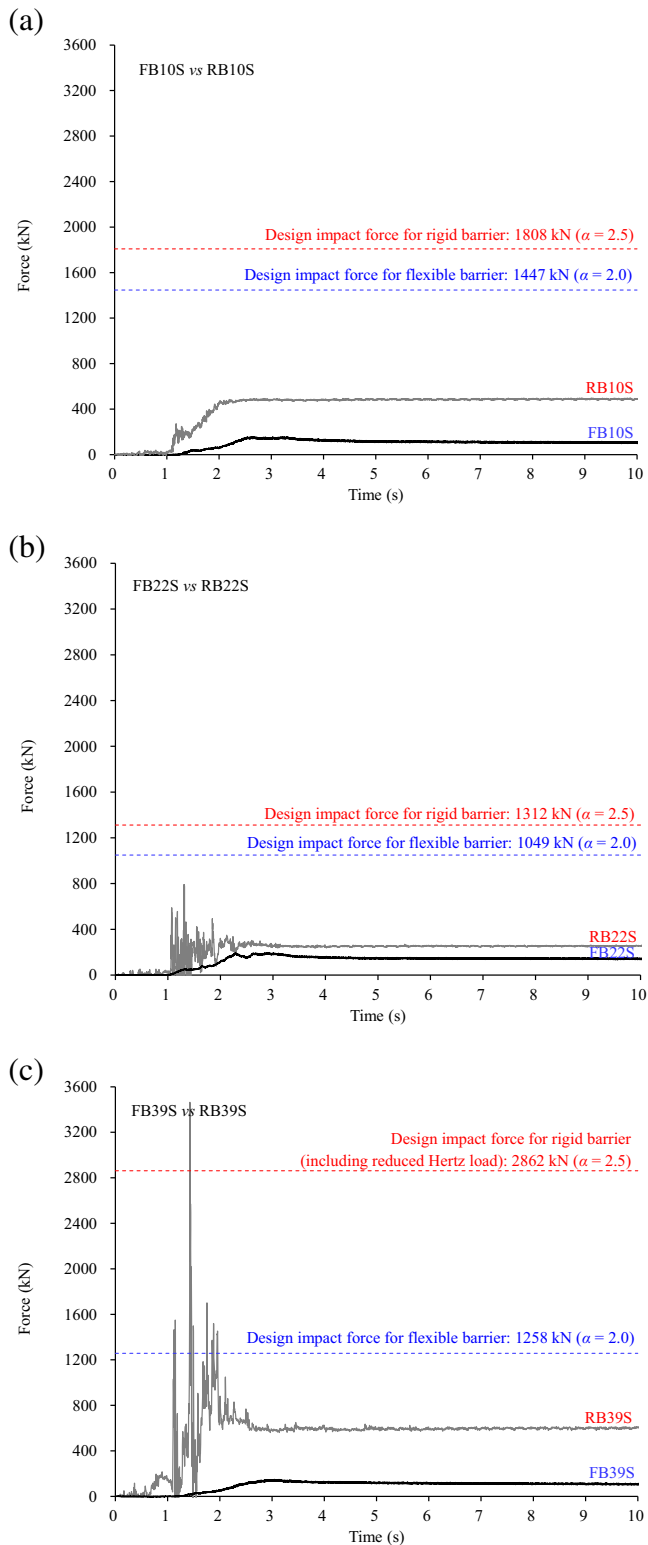


Fig. 9 Comparison of normal impact forces induced by bi-disperse flow impact on flexible and rigid (Song et al. 2018a) barriers: a FB10S vs RB10S, b FB22S vs RB22S, and c FB39S vs RB39S

Figure 10b summarizes the results for the flexible and rigid (Song et al. 2018a) barrier tests together with the two-phase flow (without boulders) data points from Song et al. (2017, two-phase

on rigid barrier) and Song et al. (2018b, two-phase on flexible barrier). The abscissa is the change of momentum $m\Delta v$ observed from the high-speed imagery (Fig. 10a), and the ordinate is the measured the force impulse $F\Delta t$ from the instrumented flexible and rigid barriers. For the rigid barrier, the results indicate that the impulse of the frontal impact is roughly equal to the momentum change. By contrast, the results for flexible barrier impact indicates that only 30% of the frontal momentum (velocity) has been transferred to the deflected flexible barrier within the duration Δt . The percentage of momentum transferred to the flexible barrier should be barrier stiffness specific. Yet, what we can infer from Fig. 10b is that the load-attenuation mechanism of the flexible barrier for frontal impact originates from the barrier deflections and extended interaction duration (Bugnion and Wendeler 2010). This load-attenuation mechanism applies to both two-phase (without boulders) and bouldery debris flows.

Comparison of peak impact force

This section aims to establish a criterion for the flexible barrier: what is the maximum boulder diameter within a flow that can still allow the flow to behave as a continuum? The dynamic pressure coefficient α of the peak force can be deduced by substituting the peak force, flow velocity, and depth into Eq. (1). Figure 11 shows the relationship between the back-calculated α and particle diameter. To further apply the findings to flows with different flow depth, the boulder diameter δ is normalized by the flow depth h . Since this α is deduced directly from peak force, it absorbs the loads due to both bulk debris and boulder impact.

For the rigid barrier tests, the value of α increases as the diameter of boulder increases from 3 mm (70 mm in prototype) to 39 mm (870 mm in prototype). As a simple criterion for design of rigid barriers against bouldery debris flows, using the hydrodynamic equation (Eq. 1) with $\alpha = 2.5$ alone is able to cover the impulse load of a 1.0-m-deep flow with 0.6-m-diameter entrained boulders (Song et al. 2018a). It means that for those with normalized boulder diameter larger than 0.6, the single boulder impact should be considered separately using the Hertz contact theory (Eq. 2).

For the flexible barrier tests, the deduced value of α is not sensitive to the boulder diameter. This further reflects the effectiveness of using the flexible barrier to attenuate the impulse loads of entrained boulders. The deduced value of α for the flexible barrier impact is even below 1.0. This is because the impulse loads by boulders are all attenuated by the low stiffness of the flexible barrier, and the resulting impact load is close to the static deposition load (Figs. 8 and 9). The attenuation is especially significant for the flows with a large normalized boulder diameter (δ/h). This means that for bouldery debris flow impact on flexible barriers, the boulder impact load may not need to be considered separately for structural and geotechnical assessments. The hydrodynamic equation (Eq. 1) with $\alpha = 2.0$ for design of the flexible barrier (Kwan and Cheung 2012) is sufficient for bouldery debris flows (Fig. 11). However, the dynamic responses of bouldery debris impact must be barrier-specific. Lower barrier stiffness corresponds to larger attenuation of the impulse loads. Short-duration boulder impulse loads are the main cause of structural localized failure (see Fig. 1b, Zeng et al. 2015), while bulk debris impact is the cause of geotechnical instability of structures. In addition to installing cushioning layers (Ng et al. 2018) in front of rigid walls to reduce the impulse loads, flexible barriers offer another effective solution to bouldery debris impact.

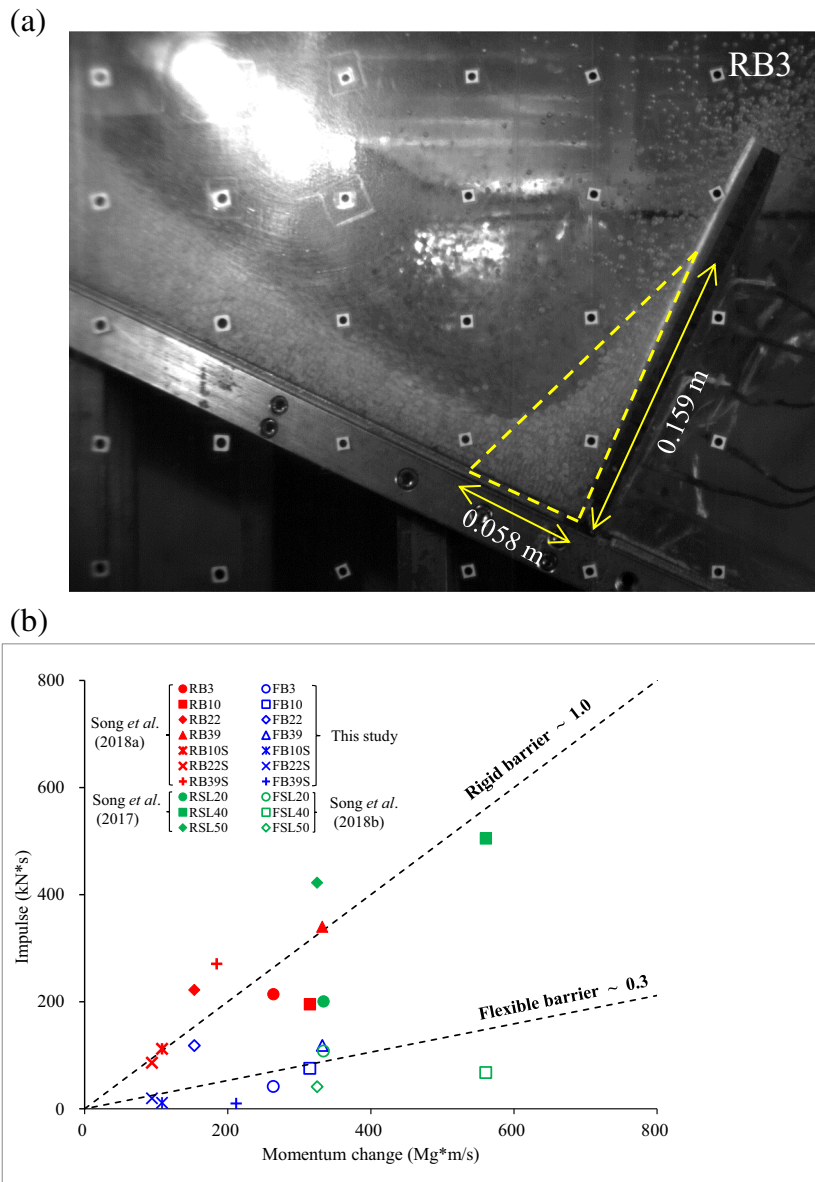


Fig. 10 a Diagram showing the representative frontal mass without obvious dead zone. b Relationship between the force impulse and change of momentum at flow front for the rigid and flexible barrier tests

State of static debris

For different debris materials, due to the distinct internal resistance and rate of energy dissipation caused by the boulder diameter and existence of fine debris, the final deposition heights and static loads on barriers differ. Moreover, discrepancy in the static loads is still observed for each rigid-flexible pair with the same debris material and similar deposition heights (Figs. 8 and 9). The flexible barrier deflects substantially (up to 22% of cable length) during the impact process, while the pile-up process induces shear stresses (Song et al. 2018b) inside the granular material. The disparity is the result of different states of the granular material, i.e., degree of proximity to the active failure state. Here, “state” means the degree of shear stress mobilization within the granular material by the pile-up process and deflection of the flexible barrier, and the “active failure state” denotes a full mobilization of the shear stresses and minimal lateral load on the barrier (Craig 2004).

Figure 12 shows the static loads of rigid and flexible barrier tests. Data points from the two-phase impact (Song et al. 2017, 2018b) are also shown for comparison. The abscissa is the theoretical active lateral load based on the Coulomb earth pressure theory and the ordinate is the measured static load. Data points lying around each dashed line fitted from the origin denote that they are at a similar state, and the data points on the diagonal line mean that the state of debris is at the active failure mode. In this way, the state of static debris with different absolute values can be compared directly.

For the bouldery debris impact, although data points are highly scattered, the measured static loads of flexible barrier tests are relatively low in magnitude and close to the diagonal line. This is because the deflection of the flexible barrier is large enough to reach the active failure state, whereas the rigid barrier tests are far away from the active failure state. For the two-phase impact, with

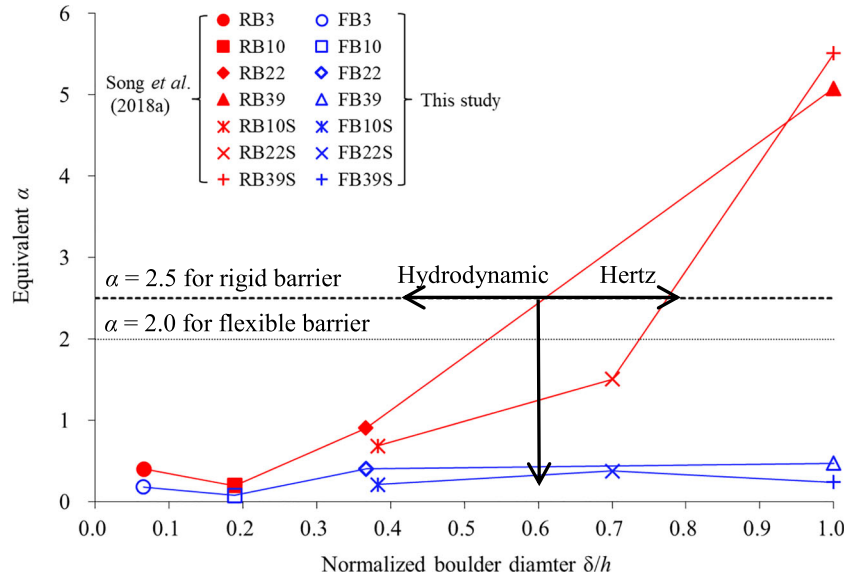


Fig. 11 Influence of particle size on the dynamic pressure coefficient α based on peak force

an increase in the solid fraction, there is an obvious trend that the debris behind the rigid barrier approaches the active state. Despite this trend, the static debris of test RS is still far away from the active state. By contrast, test FS reaches the active failure state because of the large deflection of the flexible barrier (due to the effect of low barrier stiffness). Based on the comparison between the dry bouldery debris and two-phase flow impact, the active state behind the deflected flexible barrier is only applicable to the

design of dry debris impact. The active state (minimal lateral load), as recommended by T/CAGHP (2018), is not conservative for the design of static load on debris-resisting structures.

Conclusions

Results of physical modeling impact tests using mono-disperse and bi-disperse bouldery flows have been presented in this study. The load-attenuation mechanisms of a flexible barrier in

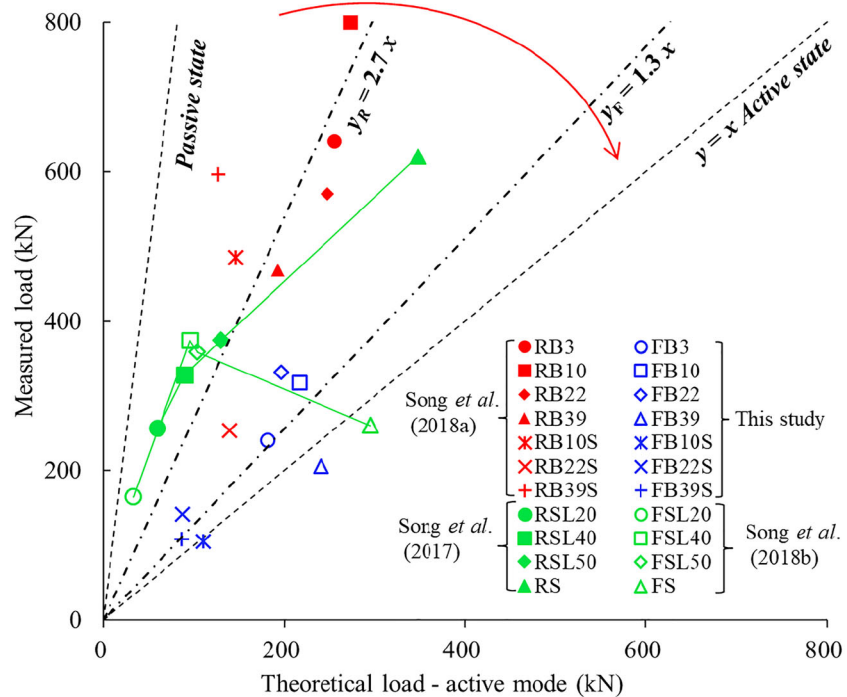


Fig. 12 Comparison of static loads on rigid and flexible barriers

mitigating bouldery debris flows are revealed by comparing the distinct dynamic responses of rigid and flexible barriers impacted by bouldery (single-phase) and two-phase (without boulders) flows. The effects of barrier stiffness are reflected by both the dynamic and static loads behind the deflected flexible barrier. Key conclusions from this study can be drawn as follows:

- (a) Large boulders generate transient impulse loads on the rigid barrier, whereas the spikes on the flexible barrier are not obvious. Compared with the rigid barrier impact, the impulse loads on the flexible barrier are significantly attenuated by the lower barrier stiffness, resulting in a “plateau” pattern of the impact time history.
- (b) The load-attenuation mechanism of the flexible barrier for the frontal impact originates from the barrier deflection and extended interaction duration. Examination of both bouldery (single-phase) and two-phase (without boulders) flows impact indicates that, for the model flexible barrier adopted in this study, only 30% of frontal momentum is transferred to the flexible barrier.
- (c) The relationship between dynamic pressure coefficient α at peak force and normalized diameter δ/h is proposed. Based on a continuum framework and from a practical point of view, this relationship defines particles with which diameter should be regarded as boulders and should be treated separately using the Hertz equation. For rigid barrier impact, with the increase in the particle size, both mono-disperse and bi-disperse flows show a clear trend of an increase in the dynamic pressure coefficient α . In contrast, for the present flexible barrier impact tests, the deduced value of α is insensitive to the boulder diameter. In the design of flexible barriers subjected to bouldery debris flow impact, the boulder impact load may not need to be considered separately from the bulk debris impact (with $\alpha = 2.0$ or even lower).
- (d) Due to the substantial deflection of the flexible barrier (up to 22% of cable length), the static dry bouldery debris behind the flexible barrier is close to the active failure state. Through comparison with the state of two-phase debris (without boulders) behind rigid and flexible barriers, it is concluded that the active failure state is only applicable to the design of dry debris impacting flexible structures.>

As a preliminary study of the load-attenuation mechanisms of the flexible barrier, only one specific and simplified barrier was used. The dynamic and static responses of the flexible barrier indeed depend on the barrier structural features (i.e., barrier stiffness and others). With the increase in barrier stiffness, the amount of momentum transferred to the barrier would increase, the boulder impact load might tend to be obvious, and the active failure state might not be fully mobilized. On the other hand, only simplified flows with spherical boulders and uniform sand were tested, which might quantitatively affect the experimental results. Further study on these two aspects is warranted to deepen the understanding of debris-barrier interaction and to optimize the structure of debris-flow flexible barrier.

Funding information This study was financially supported by the National Natural Science Foundation of China (grant nos. 51809261, 11672318, and 51709052), by a research grant (T22-603/15-N) provided by the Research Grants Council of the Government of Hong Kong SAR, China. This paper is published with the permission of the Head of the Geotechnical Engineering Office and the Director of Civil Engineering and Development, the Government of the Hong Kong SAR, China. The support by the Geotechnical Engineering Office is gratefully acknowledged.

References

- Ashwood W, Hungr O (2016) Estimating the total resisting force in a flexible barrier impacted by a granular avalanche using physical and numerical modeling. *Can Geotech J* 53(10):1700–1717. <https://doi.org/10.1139/cgj-2015-0481>
- Bugnion L, Wendeler C (2010) Shallow landslide full-scale experiments in combination with testing of a flexible barrier. In: *Monitoring, Simulation, Prevention and Remediation of Dense and Debris Flows III*, pp 161–173
- Bugnion L, McArdell BW, Bartelt P, Wendeler C (2012) Measurements of hillslope debris flow impact pressure on obstacles. *Landslides* 9(2):179–187. <https://doi.org/10.1007/s10346-011-0294-4>
- Chanson H (2004) *Hydraulics of open channel flow*. Elsevier, Amsterdam
- Costa JE (1984) Physical geomorphology of debris flows. In: *Developments and Applications of Geomorphology*. Springer-Verlag, Berlin
- Craig RF (2004) *Craig's soil mechanics*. CRC Press, Boca Raton
- DeNatale JS, Iverson RM, Major JJ, LaHusen RG, Fiegel GL, Duffy JD (1999) Experimental testing of flexible barriers for containment of debris flows. US Department of the Interior, US Geological Survey, Reston
- EOTA (2016) Flexible kits for retaining debris flows and shallow landslides/open slope debris flows. EAD340020-00-0106. <https://www.eota.eu/handlers/download.ashx?filename=ead-in-ojeu%2fead-340020-00-0106-ojeu2016.pdf>
- Gray JMNT, Tai YC, Noelle S (2003) Shock waves, dead zones and particle-free regions in rapid granular free-surface flows. *J Fluid Mech* 491:161–181
- Hübl J, Suda J, Proske D, Kaitna R, Scheidl C (2009) Debris flow impact estimation. In: *Proceedings of the 11th International Symposium on Water Management and Hydraulic Engineering*. Ohrid, Macedonia, pp 1–5
- Iverson RM (2015) Scaling and design of landslide and debris-flow experiments. *Geomorphology* 244:9–20
- Johnson CG, Kokelaar BP, Iverson RM, Logan M, LaHusen RG, Gray JMNT (2012) Grain-size segregation and levee formation in geophysical mass flows. *J Geophys Res: Earth Surf* 117(F1)
- Koo RCH, Kwan JSH, Ng CWW, Lam C, Song D, Pun WK (2016) Velocity attenuation of debris flows and a new momentum-based load model for rigid barriers. *Landslides* 14(2):617–629. <https://doi.org/10.1007/s10346-016-0715-5>
- Kwan JSH (2012) Supplementary technical guidance on design of rigid debris-resisting barriers. GEO Report No. 270. Geotechnical Engineering Office, HKSAR Government
- Kwan JSH, Cheung RWM (2012) Suggestion on design approaches for flexible debris-resisting barriers. Discussion note DN1/2012. Geotechnical Engineering Office, HKSAR Government
- Kwan JSH, Sze EHY, Lam C (2018) Finite element analysis for rockfall and debris flow mitigation works. *Can Geotech J*. <https://doi.org/10.1139/cgj-2017-0628>
- Mavrouli O, Corominas J (2010) Vulnerability of simple reinforced concrete buildings to damage by rockfalls. *Landslides* 7(2):169–180
- McArdell BW, Bartelt P, Kowalski J (2007) Field observations of basal forces and fluid pore pressure in a debris flow. *Geophys Res Lett* 34(7). <https://doi.org/10.1029/2006GL029183>
- Ng CWW (2014) The state-of-the-art centrifuge modelling of geotechnical problems at HKUST. *J Zhejiang Univ SCIENCE A* 15(1):1–21
- Ng CWW, Song D, Choi CE, Koo RCH, Kwan JSH (2016) A novel flexible barrier for landslide impact in centrifuge. *Géotechnique Lett* 6(3):221–225
- Ng CWW, Su Y, Choi CE, Song D, Lam C, Kwan JSH, Chen R, Liu H (2018) Comparison of cushioning mechanisms between cellular glass and gabions subjected to successive boulder impacts. *J Geotech Geoenviron* 144(9):04018058

- Sasiharan N, Muhunthan B, Badger TC, Shu S, Carradine DM (2006) Numerical analysis of the performance of wire mesh and cable net rockfall protection systems. *Eng Geol* 88(1):121–132
- Savage SB (1984) The mechanics of rapid granular flows. *Adv Appl Mech* 24:289–366
- Savage SB, Hutter K (1989) The motion of a finite mass of granular material down a rough incline. *J Fluid Mech* 199:177–215
- Schofield AN (1980) Cambridge geotechnical centrifuge operations. *Geotechnique* 30(3):227–268
- Song D, Ng CWW, Choi CE, Zhou GGD, Kwan JSH, Koo RCH (2017) Influence of debris flow solid fraction on rigid barrier impact. *Can Geotech J* 54: 1421–1434
- Song D, Choi CE, Zhou GGD, Kwan JSH, Sze HY (2018a) Impulse load characteristics of bouldery debris flow impact. *Géotechnique Lett* 8(2):111–117
- Song D, Choi CE, Ng CWW, Zhou GGD (2018b) Geophysical flows impacting a flexible barrier: effects of solid-fluid interaction. *Landslides* 15(1):99–110
- Sze EHY, Koo RCH, Leung JMY, Ho KSS (2018) Design of flexible barriers against sizeable landslides in Hong Kong. *HKIE Trans* 25(2):115–128
- T/CAGHP (2018) Specification of design for debris flow prevention. 021–2018. China University of Geosciences Press, Beijing
- Taylor RN (1995) *Geotechnical centrifuge technology*. Blackie Academic Professional, Glasgow, U.K.
- Wendeler C, McArdell BW, Rickenmann D, Volkwein A, Roth A, Denk M (2006) Field testing and numerical modeling of flexible debris flow barriers. In: *Proceedings of international conference on physical modelling in geotechnics*, Hong Kong
- Wendeler C, Volkwein A, McArdell BW, Bartelt P (2019) Load model for designing flexible steel barriers for debris flow mitigation. *Can Geotech J* 56(6):893–910. <https://doi.org/10.1139/cgj-2016-0157>
- WSL (2009) Full-scale testing and dimensioning of flexible debris flow barriers. In: *Technical report 1–22*. WSL, Birmensdorf
- Yong ACY, Lam C, Lam NT, Perera JS, Kwan JSH (2019) Analytical solution for estimating sliding displacement of rigid barriers subjected to boulder impact. *J Eng Mech* 145(3):04019006
- Zeng C, Cui P, Su Z, Lei Y, Chen R (2015) Failure modes of reinforced concrete columns of buildings under debris flow impact. *Landslides* 12(3):561–571

D. Song · G. G. D. Zhou 

Key Laboratory of Mountain Hazards and Earth Surface Process/Institute of Mountain Hazards and Environment,
Chinese Academy of Sciences,
Chengdu, China
Email: gordon@imde.ac.cn

D. Song
e-mail: drsong@imde.ac.cn

D. Song · G. G. D. Zhou
University of Chinese Academy of Sciences,
Beijing, China

D. Song · C. E. Choi · C. W. W. Ng
Department of Civil and Environmental Engineering,
Hong Kong University of Science and Technology,
Clear Water Bay, Kowloon, Hong Kong

C. E. Choi
e-mail: ceclarenc@ust.hk

C. W. W. Ng
e-mail: cecwwng@ust.hk

C. E. Choi
The HKUST Jockey Club Institute for Advanced Study,
Kowloon, Hong Kong

J. S. H. Kwan · H. Y. Sze
Geotechnical Engineering Office,
Civil Engineering and Development Department, Government of the HKSAR,
Hong Kong, China

J. S. H. Kwan
e-mail: juliankwan@cedd.gov.hk

H. Y. Sze
e-mail: erichysze@cedd.gov.hk

Y. Zheng
State Key Laboratory of Geomechanics and Geotechnical Engineering, Institute of Rock and Soil Mechanics,
Chinese Academy of Sciences,
Wuhan, China
e-mail: yzheng@whrsm.ac.cn